Principal image decomposition for multi-detector backscatter electron topography reconstruction

Jan Neggers, Eva Héripré, Marc Bonnet, Denis Boivin, Alexandre Tanguy, Simon Hallais, Fabrice Gaslain, Elodie Rouesne, Stéphane Roux

Version of Record: https://www.sciencedirect.com/science/article/pii/S0304399120303405
Manuscript_4399851c12fe364f9b0494d3d98a7585

Principal image decomposition for multi-detector backscatter electron topography reconstruction

Jan Neggers[a,1], Eva Héripré[a], Marc Bonnet[b], Denis Boivin[c], Alexandre Tanguy[d], Simon Hallais[d], Fabrice Gaslain[e], Elodie Rouesne[f], Stéphane Roux[b]

[a] *MSSMat, CentraleSupélec / CNRS / Université Paris-Saclay, Gif-sur-Yvette, 91190, France*
[b] *LMT, ENS Cachan / CNRS / Université Paris-Saclay, Cachan, 94235, France*
[c] *Onera, Châtillon, 92320, France*
[d] *LMS, CNRS / École Polytechnique, Palaiseau, 91128, France*
[e] *Centre des Matériaux, Mines Paristech, Evry, 91003, France*
[f] *Centre CEA de Saclay, CEA, Gif-sur-Yvette, 91191, France*

Abstract

Scanning Electron Microscopes (SEMs) often generate images with a shaded appearance which gives a natural 3D impression. Ergo, quite a few methods to reconstruct the 3D surface topography from these using shape-from-shading methods are available in the literature. Here, a novel approach is discussed which uses BackScatter Electron (BSE) images from multiple detectors to reconstruct the topography. Classically, algorithms exist which resort to a quad-BSE detector setup. However, other detector configurations are often found in SEMs. A set of images of these non-conforming detectors still contains enough information to allow for reconstruction, but requires a more general algorithm to do so. This article discusses a method based on a modal decomposition of the principal image components. The resulting method is shown to be efficient and independent of the number of detectors or their orientation. In fact, the orientation is identified as part of the algorithm and thus requires very little calibration.

Keywords: Scanning Electron Microscopy, Topography Reconstruction, Back Scatter Electron, **Principal Component Analysis**

*Corresponding author
Email address: jan.neggers@centralesupelec.fr (Jan Neggers)

1. Introduction

Typical Scanning Electron Microscope (SEM) images express a surprisingly natural topographical shading quality, allowing the beholder to mentally reconstruct the topography. This is true for images acquired with the ubiquitous Secondary Electron (SE) detector, but also for acquisitions using the Back-Scatter Electron (BSE) detector. Indeed, not long after the introduction of the SEM, methods were developed to exploit this contrast for reconstructing the topography of the sample, [3, 10].

Having access to the 3$^{\text{rd}}$ dimension is invaluable when studying mechanics of materials. Being able to visualize the topography in 3D greatly enhances our intuition for the mechanics at play. However, quantifying out-of-plane motion often allows the picture to be completed, thereby allowing more questions about the underlying mechanics be answered. The key importance when studying micro-mechanics is the ability to capture the sample kinematics *in-situ*, allowing the exploration of the mechanics as the sample deforms under load, [11].

Arguably the most common way to get access to microscopic topography information is a Scanning Probe Microscope (SPM), like for instance an Atomic Force Microscope or a Scanning Tunneling Microscope. The method proposed in this paper is not intended to compete with the latter ones in terms of accuracy and resolution. However, in the setting of an *in-situ* experiment, the SEM is more versatile and viable as it more freely allows imaging a sample that is being loaded by a testing device. Moreover, SEMs typically have a much wider magnification range, especially at the low end. Allowing also measurements of larger samples, with larger variations in topography. The proposed method is presented here as a tool that can be used in conjunction with *in-situ* SEM microscopy requiring only limited additional effort, and hence providing a very fine time resolution.

SEM based topography reconstructions can be categorized in two groups (See Tafti et al. [14] for an overview); (*i*) multi-view, (*ii*) shape from shading. The first uses similar methods as used in stereo photography, by imaging the

sample at two distinct angles the observed parallax can be used to infer the topography, [1, 2, 4, 6, 15]. These methods have been used to great success but require the sample stage to be tilted to a known angle which is often prohibitive when a loading setup is mounted on the sample stage. The proposed method in this article falls in the second class. These methods use the shading visible in the image to infer the slope of the sample and thereby reconstruct the topography, [16]. This can be performed on SE images [12], however, the most common version of this method is the "four-quadrant BSE" method, [3, 7]. In this method, the gray level images $A_i(\underline{x})$ obtained by four diagonally opposed BSE detectors $i = [1, 2, 3, 4]$ are used (as shown in Figure 1a). Let the detectors 1-3 and 2-4 form two orthogonal pairs of diagonally opposed detectors. Then two gradient images can be constructed by,

$$z_{,1}(\underline{x}) = a\frac{A_3(\underline{x}) - A_1(\underline{x})}{A_3(\underline{x}) + A_1(\underline{x})}, \qquad z_{,2}(\underline{x}) = a\frac{A_4(\underline{x}) - A_2(\underline{x})}{A_4(\underline{x}) + A_2(\underline{x})}, \tag{1}$$

where $z_{,1}$ and $z_{,2}$ are the topography gradients in the directions aligned with their respective diagonals and the parameter a is a calibration parameter to transition from gray levels to height, e.g. micrometers. From these two gradient images the topography $z(\underline{x})$ can be computed by integration. The key advantage of this method is that, the difference between data from opposing detectors, Eq. (1), cleverly cancels nearly all of the compositional contrast in the images.

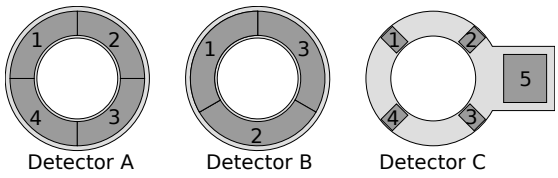

Figure 1: The three detectors configurations found in the three SEM microscopes used in this article (not to scale).

Currently, SEMs are often equipped with different BSE detector arrangements, (as shown in Fig. 1), which do not allow for a straightforward difference between opposing images. However, many of these detector arrangements, still express significant topographical contrast, suggesting that it is still possible to

reconstruct the topography. The method proposed in this article is a simple and computationally efficient way to extract the two gradient images just like in the "four-quadrant" method, even for different detector configurations. **The main advantage of the proposed method is that it is not limited to the standard "four-quadrant" detector geometries but works for a much wider range of detector clusters as long as there are at least three sections that are at sufficiently distinct orientations with respect to the sample.**

The key idea in the proposed method is that the first three principal components in the set of images will very likely give access to the following:

- $c(\underline{x})$, compositional contrast,
- $z_{,\eta_1}(\underline{x})$, topographical contrast in direction $\underline{\eta}_1$,
- $z_{,\eta_2}(\underline{x})$, topographical contrast in direction $\underline{\eta}_2$,

After aligning the obtained gradient images with the image frame, the latter two can be integrated to obtain the topography. The main advantages of the proposed method is that it is rather detector configuration agnostic. It will be shown that it is nicely suited to different configurations of 3, 4 and 5 detectors (shown in Figure 1) even if they are dissimilar in size or sensitivity.

2. Experimental data

The proposed method can be decomposed in a few steps, each will be detailed next. However, it was chosen to explain them using an example. Therefore, first the experimental data is introduced, from which one case will be picked to detail the steps.

2.1. Test cases

Six example cases were chosen to highlight the capabilities of the proposed method. The images as acquired from the first detector for each case are shown in Figure 2. Cases **C1** to **C4** were acquired on a FEI Helios NanoLab dual beam

SEM with a 3-sector BSE detector. Case **C5** was acquired on a Zeiss Sigma 300 with a 5-sector BSE detector, while Case **C6** was captured on a Zeiss Merlin 60 with a 4-sector BSE detector, see Figure 1.

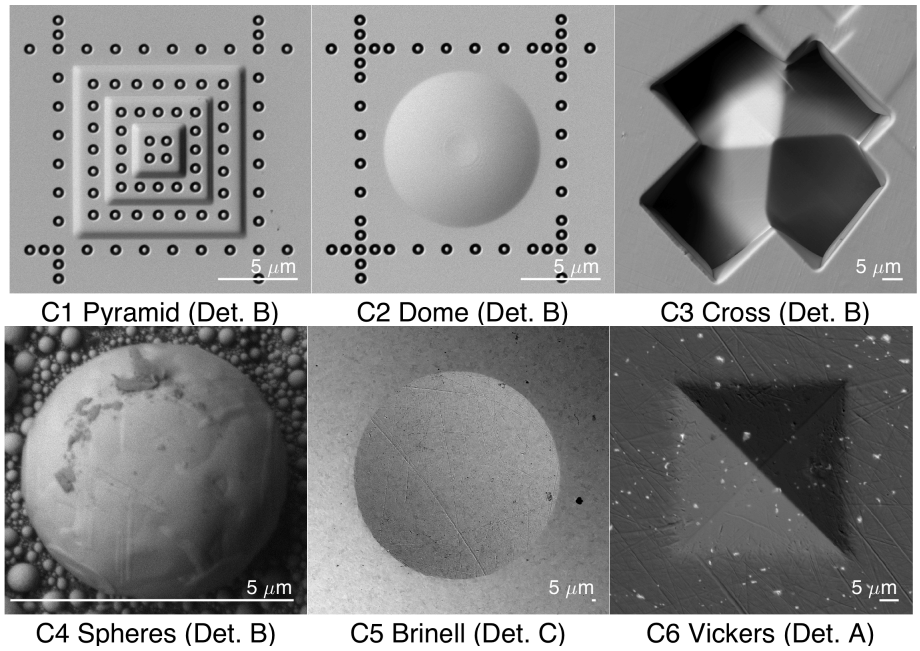

Figure 2: The 6 cases that will be discussed in this article. Each with their respective detector configuration given in parentheses.

Cases **C1** and **C2** are acquisitions of a calibration sample manufactured by M2C[1] **the manufacturing details of which are discussed in [13]**. In summary, the sample consists of a 6 mm square silicon chip mounted on 12 mm square aluminum substrate. On the silicon a topography is created by a combination of FIB (Focused Ion Beam) deposition and milling and consists of a composite of carbon and platinum. Using this method, four topographies were created in a 70 µm square area, three of which are three-step pyramids (one is **C1**) and the fourth is a dome shaped element (**C2**). **The step pyramids and the dome are convex shapes, i.e. with their summit above the**

[1]Microscopy Measurement & Calibration, http://www.m2c-calibration.com

substrate plane. However, the small circular markers are concave with their valleys below the substrate plane. The pyramid steps are 600 nm high while the dome is 1000 nm high. In total there are 308 markers with a diameter of 600 nm and a depth of 120 nm. It is these markers which serve as the calibration targets with their positions measured by means of a long-range Scanning Probe Measurement (SPM) [5].

The calibration markers have a particular form, with a rather deep ring-shaped indentation surrounding the marker. As will be discussed later on, these deep features tend to trap electrons and thereby complicate the reconstruction locally. Since this local area is completely enclosing the calibration marker, the reconstructed markers may be the locations where the proposed method is least accurate. Therefore, the full-field SPM data will be used in the following to compare the reconstructions to. This full-field data is provided by the sample manufacturer at a definition of 1026 by 1038 pixels with a pixel size of 41 nm. However, it should be considered that this full-field SPM data is less precise than the measurements of the calibration markers due to possible scanning artifacts [13].

Cases **C3** to **C5** are included to show the limits of the methodology. **C3 is made by Focused Ion Beam (FIB) milling the 4 sides of a pyramid into an amorphous metal alloy substrate thereby creating a cross-shaped excavation zone, hence the sample is named "Cross". The vertical slopes that make the outer contour of the cross-shape result in deep features. These features, like the landmarks, trap electrons, an effect which is not taken into consideration in the reconstruction method. Consequently, the reconstruction method will generate some significant artifacts at these locations. C4** are tin spheres on a silicon substrate. These samples are often supplied with SEMs for calibration. Obviously, it is not possible to reconstruct the bottom part of the sphere. However, it is interesting to evaluate how the reconstruction method fails in these impossible situations. **C5** considers a Brinell indent, made with a 10 mm indenter pressed in a steel substrate to a depth of 30 µm. Due to the low magnification of this case, the flat

surface around the indent shows a gradient in the gray level. This is typically not taken into account in many of the reconstruction methods. Finally, **C6** shows a bi-phase material, indented with a Vickers indent up to a depth of 1 µm. **This case uses the typical 4 quadrant setup, which the proposed method accepts as well as the other presented detector configurations. Consequently, this case will be used extensively to validate the proposed reconstruction algorithm against the standard four-quadrant method.**

3. Methodology

In the following, the proposed 3D reconstruction algorithm will be detailed. To visualize intermediate results of the algorithm, case C6 is chosen as an example. The case is the most straight forward due to the combination of the more familiar "four-quadrant" detector layout and the common Vickers indentation shape. However, it is emphasized that the proposed algorithm can be applied to a large variety of cases.

3.1. Principal Component Images

The key assumption underpinning the classical "four-quadrant" method is that the observed intensity at each detector depends linearly on the angle between the surface normal and the direction towards the detector. Generally, this assumption implies that the angular distribution of back scattered electrons is purely diffuse. This assumption is reasonable considering the typical placement of the detectors, requiring a high number of scattering events for the electrons to be redirected towards the detectors. Thereby, the intensity of BSE collected by a detector will be independent of the beam direction, and will rather depend on the relative orientation of the detector center with respect to the local surface normal. This assumption is less valid when looking at more forward angles, and is obviously unsuited to strongly structured materials giving rise to channeling effects. For the proposed method, the same linear description of the detector

intensity is assumed. This leads to an expression of the image captured by any detector i as

$$A_i(\vec{x}) = c(\underline{x})\big(1 + \underline{p}_i \cdot \underline{\nabla} z(\underline{x})\big), \qquad \forall i = 1, 2, \ldots, N. \tag{2}$$

that is, the set of images, A_i, can be described with recourse to three scalar fields: the compositional image $c(\underline{x})$ and the two topography gradients $z_{,x}(\underline{x})$ and $z_{,y}(\underline{x})$. The specific contribution of each of these fields is determined by a 2D vector-valued parameter $\underline{p}_i$ (or equivalently two scalar components). The vector $\underline{p}_i$ in the observation (x, y) plane points towards the projection of the detector center onto the plane, and its magnitude characterizes the sensitivity of the detector.

In the case of the classical four-quadrant detector configuration, assuming an identical sensitivity per detector, and a perfect alignment to the image coordinates, e.g. $\underline{p}_1 = a\underline{e}_x$, $\underline{p}_2 = -a\underline{e}_x$, $\underline{p}_3 = -a\underline{e}_y$ and $\underline{p}_4 = a\underline{e}_y$, the four detector images can be written,

$$\begin{aligned} A_1(\vec{x}) &= c(\underline{x})\big(1 + az_{,x}(\underline{x})\big), \\ A_2(\vec{x}) &= c(\underline{x})\big(1 + az_{,y}(\underline{x})\big), \\ A_3(\vec{x}) &= c(\underline{x})\big(1 - az_{,x}(\underline{x})\big), \\ A_4(\vec{x}) &= c(\underline{x})\big(1 - az_{,y}(\underline{x})\big), \end{aligned} \tag{3}$$

from which, one easily deduces Eq. 1. In the following, no assumption will be made about the symmetry of the detector arrangement, nor about the sensitivity or each sensor. From (2), the entire set of images can be seen as a weighted sum of three scalar fields, $c(\underline{x})$ and $c(\underline{x})\underline{\nabla} z(\underline{x})$. Assuming that over the entire gray level dynamics of the images, the difference between two images is only a small fraction of any of them (say the average), then these contributions can be retrieved from a modal decomposition such as the Principal Component Analysis (PCA), where $c(\underline{x})$ should be the dominant mode. The gradation between the different modes can be read from the eigenvalues of the PCA decomposition. Moreover, assuming a statistical isotropy of the observed surface, the second and third eigenvalues should be very close in magnitude. Finally, if more than

three detectors are used, the eigenvalues beyond the third should ideally be null.

The principal component images φ are computed from the acquired images A_i for all N detectors, by constructing the covariance matrix of the images,

$$F_{ij} = \int_{\Omega} A_i(\vec{x}) A_j(\vec{x}) \, \mathrm{d}\vec{x}, \qquad \forall i, j = 1, 2, \ldots, N, \tag{4}$$

where Ω is the field of view. This matrix can then be diagonalized and decomposed into a diagonal matrix of eigen values $[\Lambda]$ and a matrix with all eigenvectors concatenated column wise $[V]$.

$$[F] = [V][\Lambda][V]^{-1}, \qquad \lambda_i = \Lambda_{ii}. \tag{5}$$

The principal component images φ_i are then obtained by projecting the acquired images with the eigenvectors,

$$\varphi_i = \sum_{j=1}^{N} V_{ij} A_j. \tag{6}$$

The images A are deliberately not corrected for the mean, as is typical in Principal Component Analysis (PCA), to ensure that the first principal component image corresponds to the signal that is equally present in all images, i.e. the compositional information. Consequently, the next two principal component images contain the data orthogonal to the compositional information, i.e. the topographical information. If more than three images are applied in this method, the following principal images typically contain information that is more weakly correlated, such as noise or other artifacts.

Figure 3 shows the principal component images for case **C6**. For the first principal image φ_1, all contrast related to the indent is nearly erased leaving only the contrast related to the material phase information. The square area of the indent is slightly darker, indicating that, on average, less electrons were back-scattered from this area. This is expected, and is a non-linear effect that is not included in the model. The second and third principal images, φ_2 and φ_3, clearly are expressions of the surface gradient. However, they require scaling with the first principal image for them to be relative to the surface gradients.

The fourth principal image φ_4 contains the signal that is remaining. This case contains four images, and thus four principal component images can be constructed. Optimistically, the fourth principal component image only contains acquisition noise. Clearly, φ_4 contains more than just noise, where in this example the signal is consistent of that of some rigid body motion. This particular microscope did not allow the simultaneous acquisition of all BSE detectors. Thus, four separate scans were performed, and likely, the sample drifted slightly during these scans which would explain the observed fourth principal component image. Such an interpretation is also supported by the "bright/shadowed" aspects of some spots present in the second and third modes. This is a typical manifestation of motion.

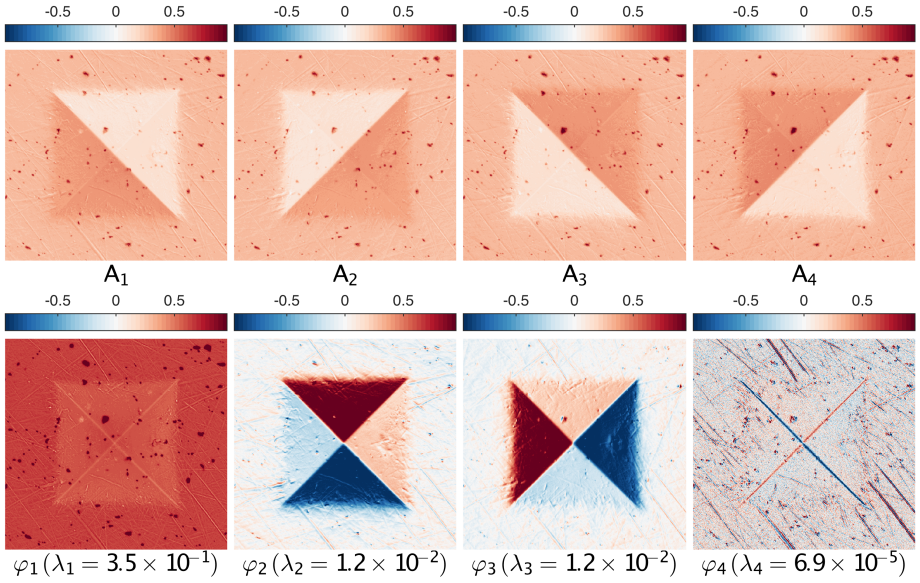

Figure 3: The four acquired images for **C6**, top row, and the four respective principal images, bottom row.

Depending on the required accuracy of the reconstruction this artifact can be ignored or not. One way to circumvent these types of artifacts is to avoid sample drift by letting the system find its equilibrium or by using an SEM that allows simultaneous acquisition of all BSE detectors. However, it is possible

to enrich the proposed method to allow small displacement corrections. The previous model can be expanded to include an unknown rigid body translation that is parameterized as one displacement vector $\underline{u}_i$ per detector,

$$\hat{A}_i(\vec{x}) = A_i(\vec{x} + \underline{u}_i) \approx A_i(\vec{x}) + A_{i,x}u_{xi} + A_{i,y}u_{yi} \qquad \forall i = 1, 2, \ldots, N.$$

where $\hat{A}$ is the representation of the acquired image at the correct position. This image can be approximated from the acquired image using a first order Taylor expansion. Rephrasing this enriched representation in the principal component framework means that the set of images is now expanded with the gradient images $A_{i,x}$ and $A_{i,y}$ raising the number of images from N to $3N$.

Figure 4 shows the principal images φ_4 to φ_7 after making the above enhancement to the method. The first three principal images are not shown because they did not change significantly to be visually different. Contrastingly, the fourth principal image did change significantly. Its contrast is now split into four contributions which correspond to the motion of the composition map (φ_4 and φ_5 look like two components of the gradient of φ_1) and the motion of the topography (mostly surface scratches) (φ_6 and φ_7). These principal images are not especially interesting by themselves. However, they do improve the reconstruction since the signal in these principal images is properly separated from the first three principal images.

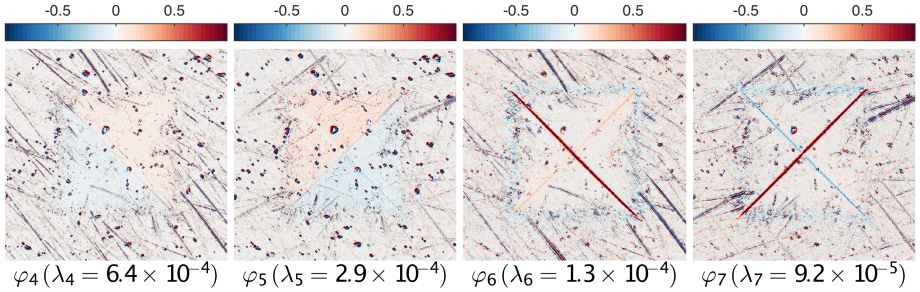

Figure 4: Four new principal images φ_4 to φ_7 obtained by including the gradient images in the principal image analyses. The image contrast is enhanced for clarity.

185 *3.2. The Gradient Images*

Within the linear framework presented in the previous section, the first three principal images are related to the three images of interest,

$$\begin{aligned} c &\propto \varphi_1, \\ z_{,\underline{\eta}_1} &\propto \varphi_2/\varphi_1 = G_1, \\ z_{,\underline{\eta}_2} &\propto \varphi_3/\varphi_1 = G_2, \end{aligned} \tag{7}$$

where $\underline{\eta}_1$ and $\underline{\eta}_2$ are two yet unknown directions.

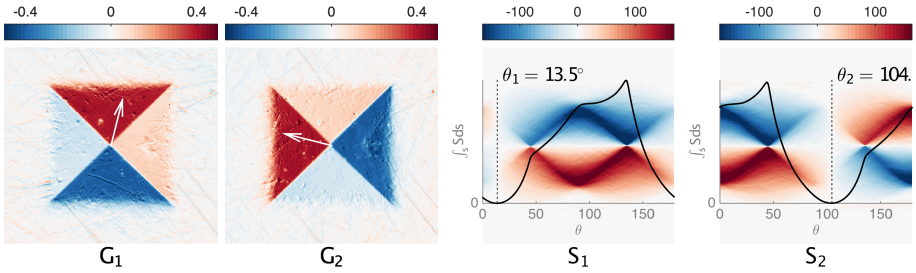

Figure 5: The two gradient images G_1 and G_2 with the direction of the gradient indicated by the arrow in the center and their respective sinograms S_1 and S_2 overlayed with their respective square integral curves, the minimum of this curve is where the gradient angle is obtained.

To reconstruct the topography, an integration step is required which will be discussed later on. To facilitate this step, the above gradients require reorientation to the x and y directions. For this reorientation, first the current gradient directions have to be found. In many cases it would be possible to deduce these directions with some knowledge of the shape of the observed object. However, in absence of such, a method is proposed here that works well if the border of the image is assumed to be a single, reasonably flat, surface. In that case, there exists a direction θ_i in which the sum of the squared gradients will add up to zero. One efficient way of finding this direction is through the Radon transform,

$$S_i(\theta, s) = \int_{-\infty}^{\infty} G_i(x(z), y(z))\,\mathrm{d}z, \qquad \forall i = 1, 2, \tag{8}$$

where z are line coordinates at varying angle θ and s are coordinates orthogonal to z. The sinograms S_1 and S_2 as produced by the Radon transforms of the gradient images G_1 and G_2 are shown in figure 5. Integrating their square along the s direction (vertical in the images) as a function of the angle θ gives the curves that are overlayed on the sinograms. The minimum of each of these curves is then used to define the gradient directions, with which the gradient images G_x and G_y can be computed (see Figure 6),

$$G_x = \cos(\theta_1)G_1 + \cos(\theta_2)G_2, \qquad G_y = \sin(\theta_1)G_1 + \sin(\theta_2)G_2. \tag{9}$$

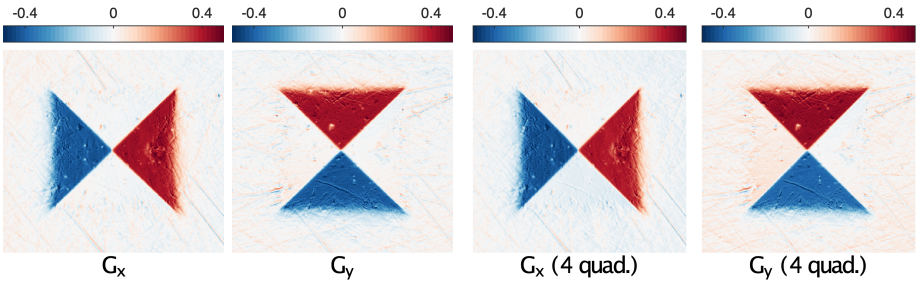

Figure 6: The two gradient images G_x and G_y after reorientation using the obtained gradient angles, θ_1 and θ_2, compared to the two gradient images obtained using the four quadrant method (1) also reoriented to the x and y directions.

The above method of obtaining the gradient angles is efficient, reasonably general but non-perfect. It is easy to image improvements to this procedure. However, the intended goal of this article is to provide a reconstruction algorithm that is more generally applicable compared to the existing methods. Further improvements to this angle finding procedure would most likely make the algorithm more precise at the cost of being less general.

Finally, the example case at hand also works for the four quadrant method. Figure 6, shows the gradient images as obtained by both methods side by side. The four quadrant gradient images as obtained using (1) will result in gradients oriented at 45°and 135°respectively since the detectors are located on

these diagonals. However, they are reoriented in the same way as (9) for easier comparison. The gradient images of the proposed method are nearly indistinguishable from the four quadrant method. This provides some confidence that the proposed method will provide a similar reconstruction quality for the classical four quadrant case, while also accepting other detector configurations. A more qualitative analysis will be performed further on for cases C1 and C2.

3.3. Topography Integration

At this stage the topography gradients are known. Integrating any of the two gradient images would lead to the topography. However, each of these integrations would be rather sensitive to noise. Therefore, a method provided by Frankot and Chellappa [8] is used instead. They formulated the problem as the solution of an optimization problem,

$$\xi^2 = \int_\Omega (z_{,x} - G_x)^2 + (z_{,y} - G_y)^2 \, \mathrm{d}\underline{x}, \tag{10}$$

where $z(\underline{x})$ is the unknown. Using the linear least squares method, that can be shown to be the optimal integration method when both $G_{,x}$ and $G_{,y}$ are affected by a white Gaussian noise, this problem reduces to solving Poisson's equation,

$$\nabla^2 z = z_{,xx} + z_{,yy} \approx G_{x,x} + G_{y,y}, \tag{11}$$

which naturally fulfills the compatibility Cauchy-Riemann condition, $z_{,xy} = z_{,yx}$, because the topography itself is chosen as the unknown. Equation (11) is then solved in the frequency domain,

$$\widetilde{z} = \frac{-i(k_x \widetilde{G}_x + k_y \widetilde{G}_y)}{2\pi(k_x^2 + k_y^2)}, \tag{12}$$

where $\widetilde{\square}$ indicates the Fourier transform, i is the imaginary unit and k_x and k_y are the wave number vectors in their respective directions. Finally, the z is obtained using the inverse Fourier transform of $\widetilde{z}$.

4. Results / Discussion

With the topography reconstruction method in place, it has been applied to the six test cases presented in section 2.1. The first two cases are of a calibrated

sample and thus allow a quantitative evaluation. The remaining four cases are included as challenging cases, showing that the method works well in a variety of cases.

Cases **C1** and **C2** both involve images of the M2C calibration sample. The manufacturer of the sample provided a full-field topographic measurement performed by SPM. This measurement is not in the same reference frame as the SEM acquisitions. Therefore a registration step is required to bring the SPM data to each of the SEM frames. For this, a simplified Digital Image Correlation (DIC) method is applied. This method is based on the Global-DIC, [9] method, however, for this case only a single four-noded quadrilateral element was applied that was of the size of the entire image. Moreover, the SPM topography image was modified to make it comparable to the sum of the BSE detector images in terms of gray level features. The low number of degrees of freedom allowed the DIC routine to robustly find the object as visible in the SEM images in the SPM image and register the two. The applied DIC registration method is considered out of the scope of this article since it is not part of the discussed algorithm. The main point of the method is that it allows to evaluate the provided SPM data at the same material points as the SEM reconstruction using the same reference frame. However, it should be noted that some of the presented errors in these comparisons may be due to registration errors.

Furthermore, the reconstructed topography is known up to an unknown gain and offset, and may be titled with respect to the SPM data. Therefore, the obtained topography is aligned to the SPM data by fitting the following four parameters,

$$z_{\mathrm{spm}} = a_0 + a_1 x + a_2 y + a_3 z. \tag{13}$$

The offset a_0 and the two tilt parameters (a_1 and a_2) are typically irrelevant, but the gain a_3 is important. It is the only calibration parameter that is required for the proposed method. It relates the gray level sensitivity to the topography gradients. This parameter depends on the SEM acquisition settings such as beam acceleration, spot size, working distance, etc. For the quantitative com-

parison at hand, these parameters are chosen to be the ones that minimizes the L_2 distance between z and z_{spm}. Consequently, the remaining error should be seen as a measure of the relative error between the two topographies.

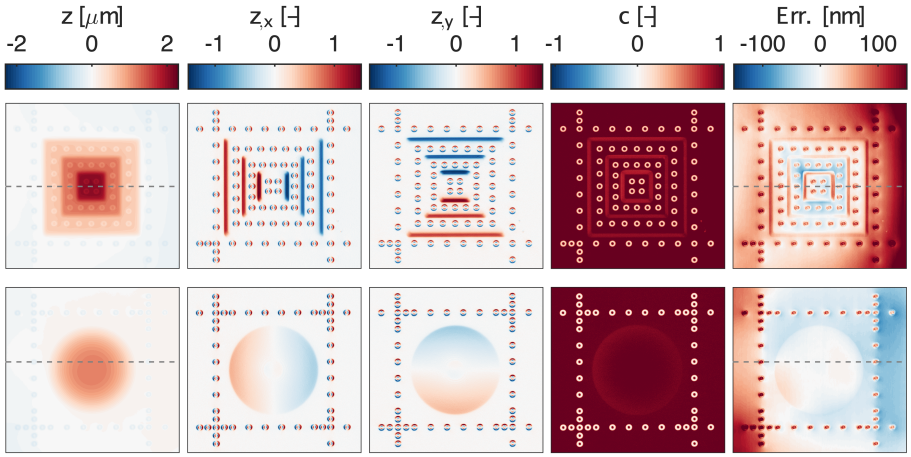

Figure 7: The results of the reconstruction for the cases **C1** (top row) and **C2** (bottom row).

Figure 7 shows the results of the topography reconstruction algorithm as applied to the cases **C1** and **C2**. These cases used the three-segment detector layout (B) as shown in figure 1. Simply being able to reconstruct the topography from these non-diagonally opposing detectors shows the main advantage of the proposed method. Moreover, on the right of figure 7 the error maps are shown. The RMS of the error maps are 77 nm and 45 nm for the pyramid and the dome respectively. **The topography profile and the corresponding error profile for a single cross-sections is shown in figure 8. The cross-section is chosen as close as possible to the summit while capturing at least a few landmarks.**

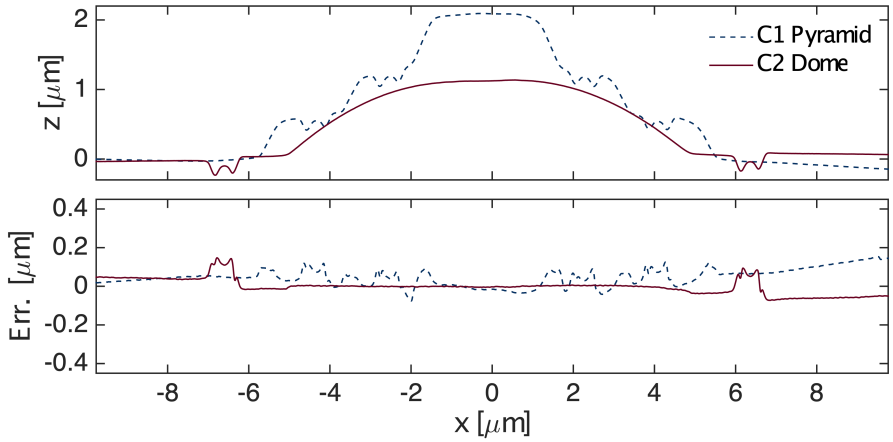

Figure 8: The topography Z and it's error Err. for cases **C1** and **C2** as a profile along the cross-sections indicated with the dashed horizontal lines in figure 7.

The error map in Figure 7 and the corresponding profiles in Figure 8 show that the major features of the samples are well captured. Contrastingly, the errors are most pronounced on the small landmarks. This was expected, as the landmarks have the highest surface gradients, as well as, some narrow features which tend to trap backscattered electrons. This is confirmed by the compositional images (4^{th} column), as they show lower values in the landmarks. These samples are manufactured by milling their shapes out of a layer of deposited platinum. Ergo, their composition should be uniform over the image. Lower values would normally indicate a lighter material which produces less back scattered electrons. However, in this case the effect is purely geometrical. These landmarks are a challenge for most reconstruction algorithms. Even though these severe features are not reconstructed perfectly, the proposed method robustly deals with them and manages to faithfully reconstruct the rest of the image.

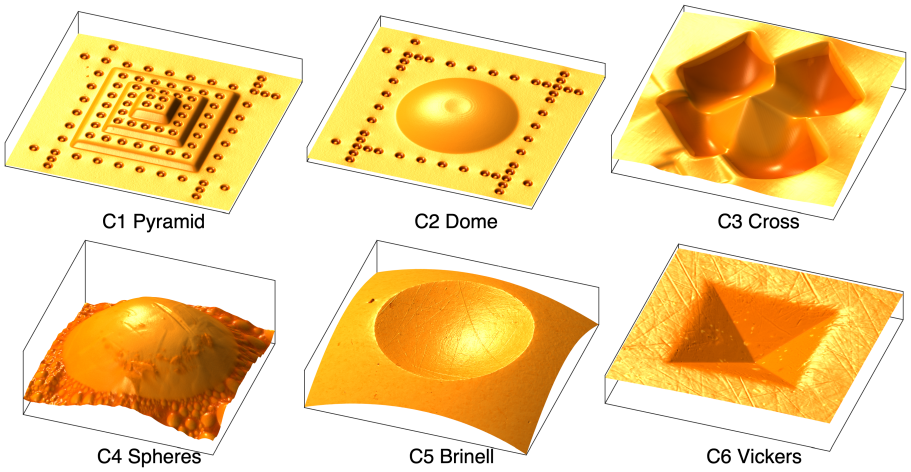

Figure 9: The reconstructed topographies of the 6 cases that are discussed in this article with the colors representing the obtained compositional map.

Figure 9 shows all six reconstructed topographies with the color map representing the compositional information. The robustness of the algorithm is sufficient to generate these reconstructions without any problems. However, the algorithm is not perfect. Any gray level contrast that is equally present in the entire image set will always be interpreted as compositional information. This typically leads to an underestimation of the slope in high slope areas or in areas that block back scattering electrons otherwise. It causes the landmarks in **C1** and **C2** to be underestimated in depth, and it curves the slopes near the bottom of the pyramid in **C3**. Conversely, any gradient in gray level that depends on the detector will be interpreted as surface curvature even if the sample was flat. **C5** is a clear example of that, the low magnification of this case creates a shading effect due to the tilting of the beam. This effect can be corrected for if the inflection point of the beam is known (which can be related to the working distance). However, such treatment is considered out of the scope of this paper. Finally, **C4** was an impossible case, as the bottom surface of the spheres cannot be reconstructed with any shape-from-shading method. However, the method does provide usable information, as the tops of the spheres are faithfully reconstructed. Nevertheless, care has to be taken when interpreting these results as

the height difference from one sphere to the next is completely unreliable. Now, it should be noted that, most of these issues are also present in the classical "four-quadrant" method, and also in other related methods. The key message is here that the proposed method is accurate under good conditions, and fails gracefully under challenging or impossible conditions.

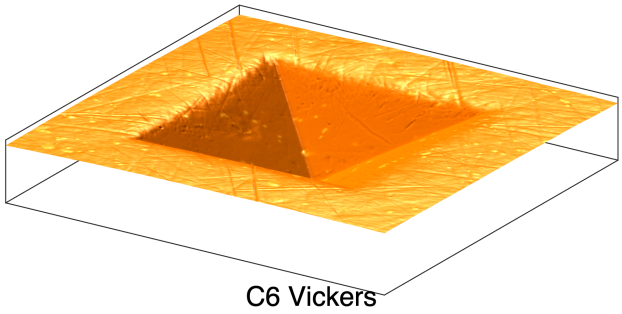

Figure 10: The reconstructed topography of **C6** now oriented such that the surface scratches catch the (rendered) light.

Although the proposed algorithm is challenged by high slopes or deep wells, a final remark is offered about the robustness of the method. The sample surface of the case C6 had surface scratches, some of which traversed the entire surface, (see Figure 10). In such a case, a severe feature segments the image into two (or more) isolated segments. Since this method is relying on integration of the gradient images, such a complete bisection may create a discontinuity along the feature. However, in all of the treated cases, when the algorithm is presented with a feature where the gray-level no longer faithfully represents the surface orientation, the resulting error remains local and does not propagate over the rest of the image. This is shown in Figure 10 as each of the disjointed planes remain reasonably co-planar.

5. Conclusions

The problem of reconstructing the 3D topography from back scattered electron images is not a new problem and many great solutions exist in the literature. However, this article proposes a novel approach to solving the problem. By recasting the acquired images into the space of principal component images, it is possible to perform the topography reconstruction even when the BSE detectors are not the typical "four-quadrant" configuration. The method was shown to work on 3, 4, and 5 detector variants, and naturally accepts BSE detectors with different or un-calibrated sensitivities. In general, the minimum number of input images is three since the output of the method is also three images, the compositional image and the two topographical gradients in the x and y directions respectively. Additional images simply improve the reconstruction by enhancing the signal and attenuating the noise.

The proposed method does not require any *a priori* knowledge on the detector placement nor sensitivity nor the acquisition settings of the SEM. As such, it is nearly calibration free. The obtained topography is known up to an unknown amplitude. This scale factor can be obtained by measuring an object of known height using the same SEM settings. This can be done before or after the experiment, but it would be preferable to position such an object in the field of view during the experiment, e.g. a nano-indent.

The accuracy of the method was shown to be of the order of 10% of the sample height. Clearly, this level of accuracy is no match when compared to scanning probe measurements. However, being a purely non-contact method may allow applications that are simply not possible in SPM systems. Moreover, often *in situ* experiments are performed inside an SEM for other reasons, and in that case it is of little additional cost to also acquire images using the BSE detectors.

Finally, the proposed method is not perfect. The linear model that relates gray level variation to surface slope is limited and is significantly deviating from reality in locations with steep slopes and in locations where diffuse scattering

is no longer a valid assumption. However, it was shown that the method tends to fail gracefully. The reconstruction artifacts are limited to these challenging areas and the rest of the image will still be accurately reconstructed.

Acknowledgments

This work has benefited from the financial support of the LabeX LaSIPS (ANR-10-LABX-0040-LaSIPS) managed by the French National Research Agency under the "Investissements d'avenir" program n°ANR-11-IDEX-0003-02, **and n°ANR-10-EQPX-37 MATMECA**.

References

[1] Beil, W., Carlsen, I. C., 1990. A combination of topographical contrast and stereoscopy for the reconstruction of surface topographies in SEM. Journal of Microscopy 157, 127–133.

[2] Carli, L., Genta, G., Cantatore, A., Barbato, G., De Chiffre, L., Levi, R., 2011. Uncertainty evaluation for three-dimensional scanning electron microscope reconstructions based on the stereo-pair technique. Measurement Science and Technology 22 (3).

[3] Carlsen, I. C., 1985. Reconstruction of True Surface-Topographies in Scanning Electron Microscopes Using Backscattered Electrons. Scanning 7, 169–177.

[4] Cornille, N., Garcia, D., Sutton, M. A., McNeill, S., Orteu, J.-J., 2003. Automated 3D reconstruction using a scanning electron microscope. In: SEM conference on experimental and applied mechanics. Charlotte, pp. 2–4.

[5] Dai, G., Pohlenz, F., Danzebrink, H. U., Xu, M., Hasche, K., Wilkening, G., 2004. Metrological large range scanning probe microscope. Review of Scientific Instruments 75 (4), 962–970.

[6] Ellison, T. P., Taylor, C. J., 1991. Calculating the surface topography of integrated circuit wafers from SEM images. Image and Vision Computing 9 (1), 3–9.

[7] Estellers, V., Thiran, J.-p., Gabrani, M., 2014. Surface Reconstruction From Microscopic Images in Optical Lithography. IEEE Transactions on Image Processing 23 (8), 3560–3573.
URL http://ieeexplore.ieee.org/document/6832559/

[8] Frankot, R. T., Chellappa, R., 1988. Method for Enforcing Integrability in Shape From Shading Algorithms. IEEE Transactions on Pattern Analysis and Machine Intelligence 10 (4), 439–451.

[9] Hild, F., Roux, S., mar 2012. Comparison of Local and Global Approaches to Digital Image Correlation. Experimental Mechanics 52 (9), 1503–1519.

[10] Lebiedzik, J., 1979. An Automatic Topographical Surface Reconstruction in the SEM. Scanning 2, 230–237.

[11] Mignot, C., 2018. Color (and 3D) for Scanning Electron Microscopy. Microscopy Today 26 (3), 12–17.

[12] Paluszyński, J., Słówko, W., 2009. Measurements of the surface microroughness with the scanning electron microscope. Journal of Microscopy 233 (1), 10–17.

[13] Ritter, M., Dziomba, T., Kranzmann, A., Koenders, L., 2007. A landmark-based 3D calibration strategy for SPM. Measurement Science and Technology 18 (2), 404–414.
URL http://stacks.iop.org/0957-0233/18/i=2/a=S12

[14] Tafti, A. P., Kirkpatrick, A. B., Alavi, Z., Owen, H. A., Yu, Z., 2015. Recent advances in 3D SEM surface reconstruction. Micron 78, 54–66.
URL http://dx.doi.org/10.1016/j.micron.2015.07.005

[15] Thong, J. T. L., Breton, B. C., 1992. In Situ Topography Measurement in the SEM. Scanning 14, 65–72.
URL pf

[16] Zhang, R., Tsai, P.-S., Cryer, J.-E., Shah, M., 1999. Shape from Shading: A survey. IEEE Transactions on Pattern Analysis and Machine Intelligence 21 (8), 690–706.